



HAL
open science

High cycle fatigue strength of additively manufactured AISI 316L Stainless Steel parts joined by laser welding

Foued Abroug, Axel Monnier, Lionel Arnaud, Yannick Balcaen, Olivier
Dalverny

► **To cite this version:**

Foued Abroug, Axel Monnier, Lionel Arnaud, Yannick Balcaen, Olivier Dalverny. High cycle fatigue strength of additively manufactured AISI 316L Stainless Steel parts joined by laser welding. *Engineering Fracture Mechanics*, 2023, 275, pp.108865. 10.1016/j.engfracmech.2022.108865 . hal-03954430

HAL Id: hal-03954430

<https://hal.science/hal-03954430>

Submitted on 24 Jan 2023

HAL is a multi-disciplinary open access archive for the deposit and dissemination of scientific research documents, whether they are published or not. The documents may come from teaching and research institutions in France or abroad, or from public or private research centers.

L'archive ouverte pluridisciplinaire **HAL**, est destinée au dépôt et à la diffusion de documents scientifiques de niveau recherche, publiés ou non, émanant des établissements d'enseignement et de recherche français ou étrangers, des laboratoires publics ou privés.

High cycle fatigue strength of additively manufactured AISI 316L Stainless Steel parts joined by laser welding

Foued Abroug^{a,*}, Axel Monnier^a, Lionel Arnaud^a, Yannick Balcaen^a, Olivier Dalverny^a

^a*Laboratoire Génie de Production (LGP), Université de Toulouse, INP-ENIT, Tarbes, France.*

Abstract

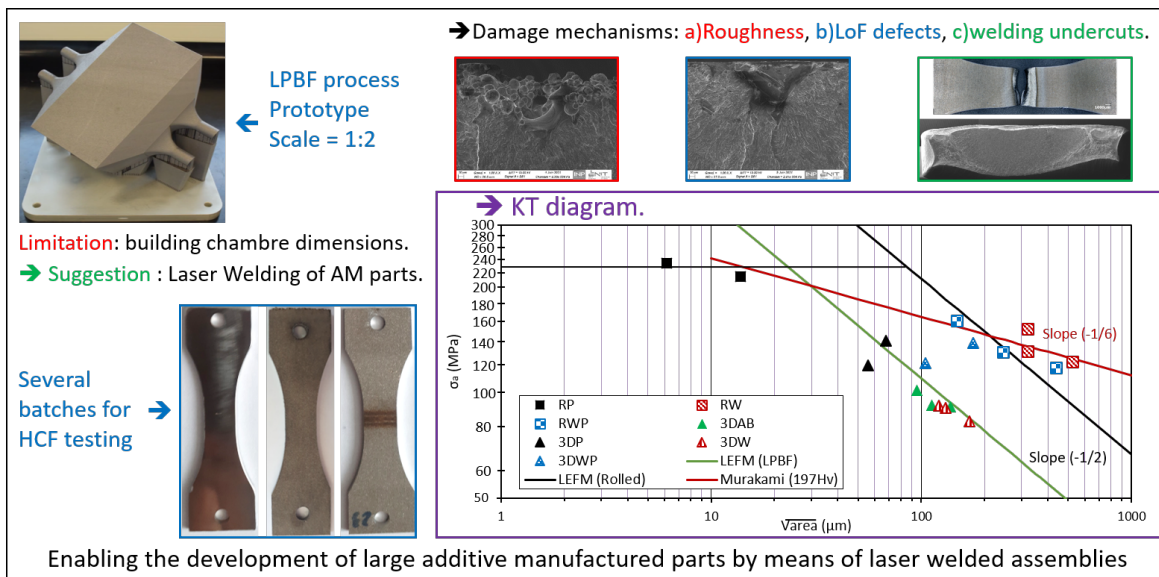
The present paper deals with the high cycle fatigue behavior of 316L stainless steel parts, obtained either by rolling or by LPBF additive manufacturing process, and their assemblies by autogenous laser welding. The aim is to study the effects of this assembly process on the fatigue strength, assessed at a 10^6 cycles, of additively produced parts, compared to that of raw rolled products. An original campaign of high cycle fatigue tests based on seven batches of specimens, manufactured additively or cold rolled, one-pieced or assembled, raw or polished, is carried out with a positive load ratio ($R= 0.1$). A stress relieving heat treatment is applied to all specimens to reduce residual stress levels. Particular attention is paid to identifying the damage mechanisms associated with each batch. Preliminary results allowed an original conclusion that laser welding does not degrade the fatigue strength of additively produced parts. In addition, the fatigue behavior of the studied system depends essentially on the stress concentration generated on the surface or a few micrometers in the underlayer, mainly by the roughness of the LPBF produced parts combined with the lack of fusion (LoF) defects, and in a second order by the geometry of the laser welding channel. Furthermore, additively produced parts showed higher sensitivity to the presence of defects than rolled parts.

Keywords: Additive manufacturing LPBF, Laser welding, Surface defect, High cycle fatigue.

Graphical abstract

*. Corresponding author. Tel. : +33 5 62 44 27 26 ; fax : +33 5 62 44 27 27

Email address: Foued.Abroug@enit.fr (Foued Abroug)



Nomenclature

ΔK_{th} threshold stress intensity factor range

$\Delta\sigma_a$ stress range $\Delta\sigma_a = 2\sigma_a$

σ_a stress amplitude

\sqrt{area} square root of the defect's area projected onto a plane perpendicular to the applied stress

a defect's depth

AMAB Additively Manufactured As-Built

AMP Additively Manufactured Polished

AMW Additively Manufactured Welded

AMWP Additively Manufactured Welded Polished

b material parameter

BM Base Metal

C material parameter

D accumulated damage

D_{50}	powder's diameter at 50% of the population
f	frequency
H_v	Vickers hardness
HAZ	Heat Affected Zone
HCF	High Cycle Fatigue
HT	Heat Treatment
K	stress intensity factor
KT	Kitagawa-Takahashi
LoF	Lack of Fusion
$LPBF$	Laser Powder Bed Fusion
LW	Laser Welding
m	number of steps
MZ	Melting Zone
N	number of cycles
N_i	number of cycles fixed at 10^6 cycles
n_i	number of cycles per step
R	load ratio
RP	Rolled Polished
RW	Rolled Welded
RWP	Rolled Welded Polished
$S\sigma_a$	loading amplitude step
SS	Stainless Steel
Y	defect's shape factor

1. Introduction

Metal additive manufacturing processes are rapidly evolving in modern industry. Laser Fusion of Powder Bed, commonly known as LPBF, is gaining more and more prominence in the production market, due to its ability to generate, from a 3D design, parts of high geometric complexity, not achievable by conventional techniques such as machining or forging, and in an almost finished state called "near net shape". This geometric freedom makes it possible, among other things, to create more efficient, lighter parts with more compact dimensions [1][2].

However, despite the progress of the LPBF process, it lacks maturity in various aspects. Among the challenges faced by this technique are the presence of manufacturing defects, such as high surface roughness of the as-built printed part [3][4], as well as internal defects created at different distances from the surface [5][6]. These defects are often at the origin of a low fatigue strength of LPBF produced parts, compared to that obtained for parts issued from other processes [6]. For example, Vayssette et al. [4] showed a 60% decrease in fatigue strength of the LPBF TA6V specimens in the as-built state compared to hot rolling.

In addition to these defects, residual stresses reaching hundreds of MPa in tension or compression are generated within the printed part due to the thermal history of the LPBF process [7]. The microstructure is also different from conventional materials, with pronounced anisotropy and columnar grains reaching a few millimeters in length in the building direction [8]. All these aspects can define a different fatigue behavior for each configuration [6].

Another challenge for the LPBF process is the limitation in terms of printable volume. The volume of parts that can be printed is limited by the dimensions of the building chamber, which is commonly a bit less than 300 mm x 300 mm x 300 mm, making large printed parts, such as one meter in size, accessible only to very few factories.

One of the solutions to limited volumes is hybrid manufacturing, which consists of assembling parts obtained either by additive manufacturing or by other conventional manufacturing processes. The assembly of parts can be performed by different techniques such as brazing, welding (arc, laser, electron beam, etc.). However, for each assembly technique, the mechanical behavior must be apprehended both in quasi-static regime and in cyclic regime before the use of the assembled

part.

Several studies have reported Laser Welding (LW), mainly in the case of rolled sheets and only a few in the case of additively manufactured parts [9][10]. The results showed that LW generates defects similar to those generated by LPBF process. First, LW results in an anisotropic microstructure at the weld zone [11]. Moreover, residual stresses in the welded zone vary drastically between tension and compression along the thickness of the welded part [12]. Studies also show that the welding process results in a topographic change on the surface presenting a bump in the middle of the weld zone and undercuts or valleys on the sides [13], as well as a population of porosity at the weld joint [12]. These porosities reach sizes of around 0.2 mm and can form clusters of around 1 mm in length in some cases [11].

As for mechanical behavior, studies show that the welded joint is at the origin of failure and defines the monotonic tensile strength of the assembly [13][14]. The elongation is reduced due to the properties of the welded material. Other studies have addressed the question of the cyclic behavior of LW parts, compared to unassembled state, but mainly in the case of rolling [11][15]. These studies show the harmfulness of the porosity population and/or the weld seam, which reduces the fatigue strength by about 50-60% [11][15]. The question of the high cycle fatigue (HCF) strength of LW parts obtained by additive manufacturing is still little addressed in the literature [16].

A recent study by Mokhtari et al. [17] addressed the impact of microstructure and surface roughness on the weldability, resultant microstructure and mechanical properties of butt joint SS 316L parts obtained by LPBF or rolling and provided a set of convenient parameters for welding such parts. The results showed that the welding has a low impact on the microstructure of the LPBF samples, that the fractures are located on the fusion zone and that the ductility decreased by around 30% compared to the rolled metal.

The present study is an extension of the work of [17] and aims to assess the high cycle fatigue behavior of SS 316L parts, obtained either by LPBF process or by rolling, and assembled by LW. The main objective is to identify the impact that LW has on LPBF produced parts in terms of high cycle fatigue strength at 10^6 cycles, for both cases. The study also focuses on the understanding of the damage mechanisms leading to the fatigue failure for each configuration.

2. Material and experimental procedure

2.1. The 316L stainless steel

In this paper, the base material is cold rolled, annealed 316L stainless steel and additively manufactured plates, both of 2 mm of thickness. The chemical composition of both feedstock materials has already been studied and detailed in the previous work of [17].

The printed plates are made using an LPBF 3D Systems ProX DMP 300 machine using a powder whose size ranges mainly between 5 and 38 μm . The D_{10} , D_{50} and D_{90} of the powder are 9.8, 20.1 and 38.1 μm respectively. The manufacturing parameters are shown in Table 1. The generated parts are shown in Fig.1 where two types of geometries are manufactured; the non welded specimens are manufactured as solid plates of 65 x 18 x 2 mm. The welded specimens however are produced in the form of half plates (130 or 150 x 34 x 2 mm) as shown in Fig.1 and then welded together. Specimens are afterwards extracted as detailed further in the text.

TABLE 1: LPBF used parameters

Power (W)	Speed (mm/s)	Hatching space (mm)	Layer thickness (mm)	Manufacturing strategy	reorientation angle ($^{\circ}$)
215	1800	0.05	0.04	Hexagonal cell	90

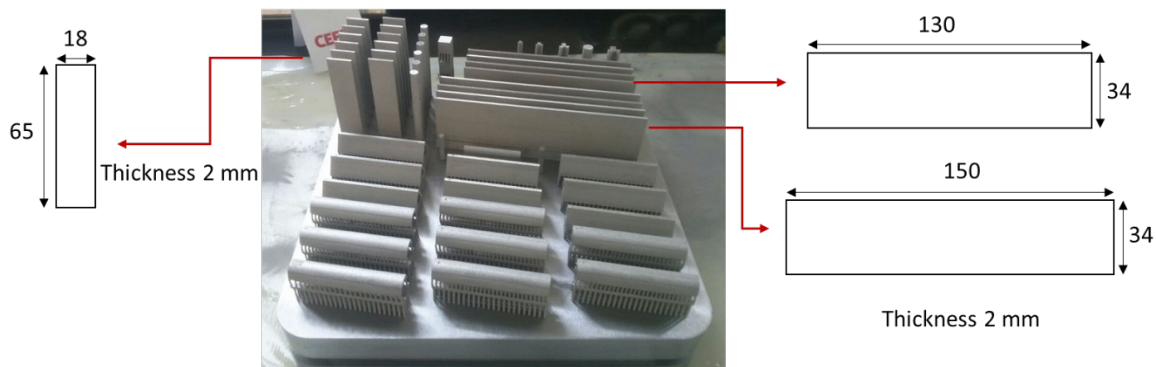


FIGURE 1: Produced parts with supported specimens in the background.

The microstructure analysis of rolled sheets and LPBF process plates has been extensively detailed in the work of [17] and is recalled in Fig.2. Let's recall that the rolled sheet's microstructure

is mainly composed of equiaxial, recrystallized and non-recrystallized grains, whereas the additively manufactured material has grains which grow along the building direction and reach a few millimeters in length, due to the thermal history during the additive process.

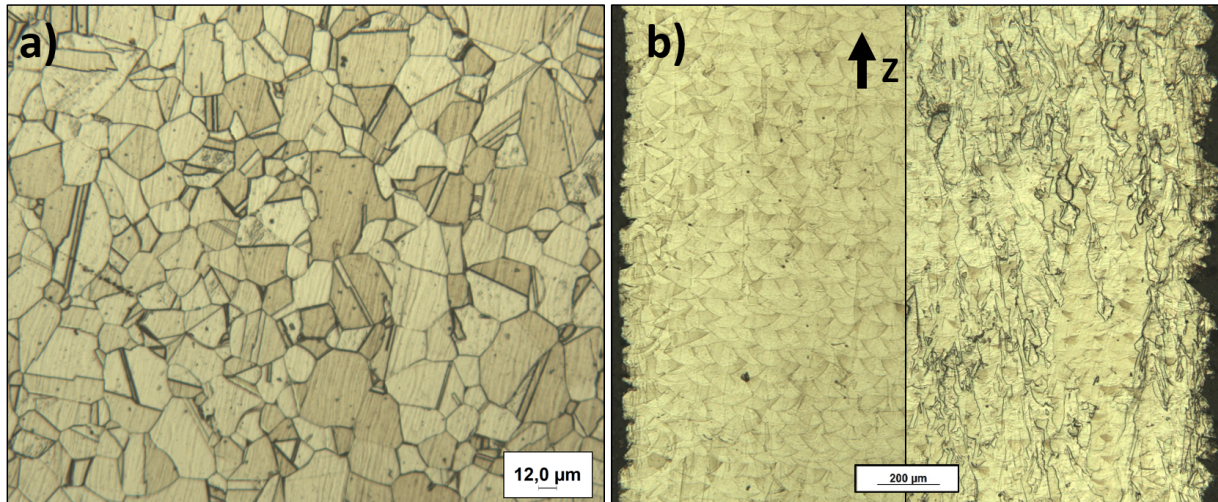


FIGURE 2: Microstructure of the SS 316L obtained by optical microscopy for a) rolled sheet part and b) additively produced material showing melt pool traces on the left and grain size and orientation on the right.

Regarding the LW for the two materials, it is carried out on a TruLaser Cell 3000 machine as detailed in [17]. Welding parameters are recalled in Table 2. The same set of parameters is used for rolled sheets and additively produced parts. The welded zone has an hourglass shape (see Fig.3) for the rolled sheet and the LPBF produced plate, with a larger upper and lower areas for the rolled sheet. This difference was attributed to the surface roughness effect on absorptivity, in addition to slight difference between chemical composition and homogeneity of feedstock material in the case of the LPBF plate [17]. The width of the fusion zone for both materials is however the same at the center of the specimen. Fig.3 also shows the presence of porosity at the weld joint for rolled sheets and additively produced plates.

Fig.4 shows scans of the surface topography for the rolled sheet and printed plate after LW. The scans are performed via a Keyence VHX-6000 numerical microscope. Fig.4-a and Fig.4-c show fairly homogeneous reinforcements with a convex shape for both rolled and AMed parts, Fig.4-b and Fig.4-d show surface scans of the back of the rolled and AMed and welded samples. It can be seen that the rolled sample still has a convex shape at the welding zone but also irregular

TABLE 2: LW parameters [17].

power (W)	speed (m/min)	Ø at focal point (μm)	Focal distance / surface (mm)	Argon flow (L/min)
1500	1	120	0.3	25

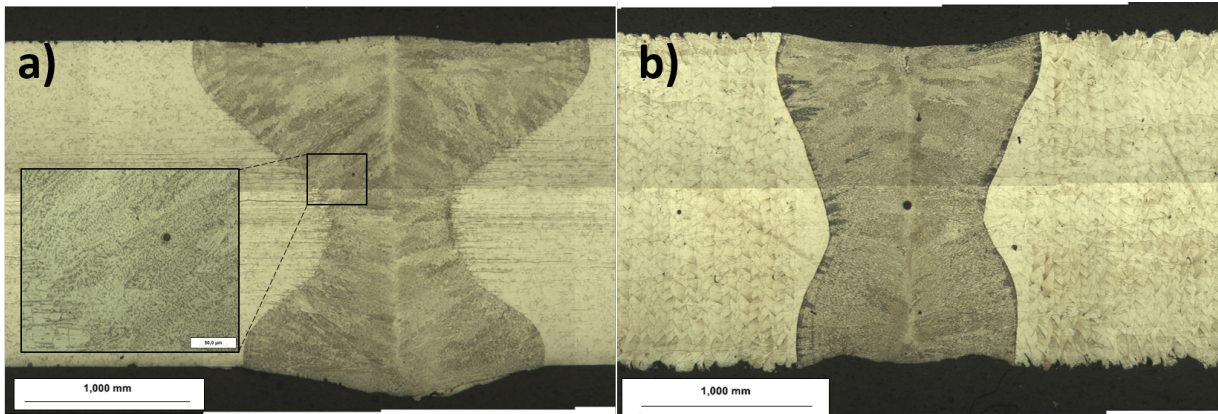


FIGURE 3: Optical microscopy observations of the welded zone for a) rolled sheet parts and b) LPBF parts [17].

undercuts, or valleys. These undercuts, with a depth between $100 \mu\text{m}$ and $200 \mu\text{m}$, can be at the origin of stress concentration and possibly affect the fatigue strength. As for the LPBF sample, a concave shape is observable with a channel of $100\text{-}150 \mu\text{m}$ in depth which would also generate stress concentration and possibly affect the fatigue strength. As detailed in [17], such difference in geometry is common in the literature [9] and is due to laser-matter interactions and to the roughness and hence absorptivity difference between AMed and rolled samples.

Monotonic tensile tests were carried out by [17] and the results are recalled in Table 3. The results showed similar behavior for the LPBF process samples before and after LW, however the elongation is reduced after welding and reaches 42%. For the rolled samples, the welding slightly enhanced the Yield stress but also reduced the elongation, which reaches 56%.

The geometry of the fatigue test specimen is designed according to the ISO1099 standard [18] and is presented in Fig.5, with a thickness of 2 mm. A post-processing stress relieving heat treatment is applied on all printed and/or welded specimens. It consists of a 300°C for 6 hours followed by air cooling. According to [19][20], it ensures no microstructural change during the

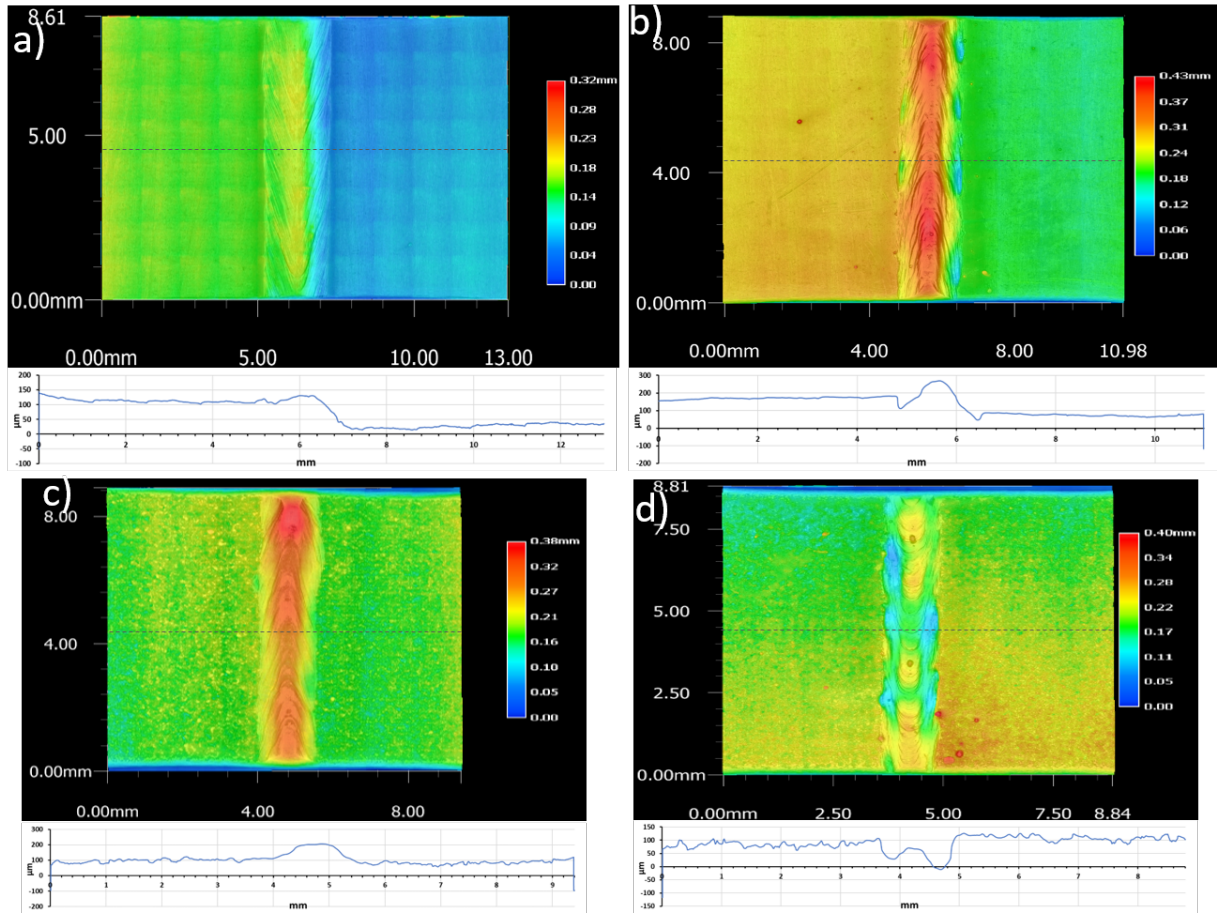


FIGURE 4: 3D surface scans of the welded zone for a) top and b) bottom of rolled sheet parts, c) top and d) bottom of LPBF parts.

TABLE 3: Monotonic properties of the SS 316L [17].

	LPBF ref	LPBF weld	Rolled ref	Rolled weld
Yield stress (MPa)	423±5	423±2	261±19	284±4
Strength (MPa)	568±5	568±2	602±2	598±3
Elongation (%)	51±1	42±14	73±6	56±3

process.

For the non welded solid plates, the specimen geometry is shaped via a high-speed machining process (See Fig.6 a and b). The welded specimens however are laser cut, after plates are laser

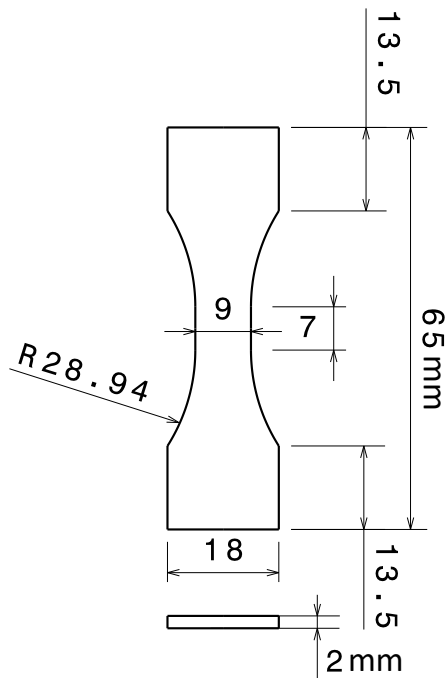


FIGURE 5: Fatigue test specimen geometry, all values are in mm.

welded, on the same machine (see Fig.6-c). Then, for all specimens, welded or not, polished or as-built, a polishing was systematically applied along their thickness and on the edges, to avoid any surface roughness induced crack initiation.

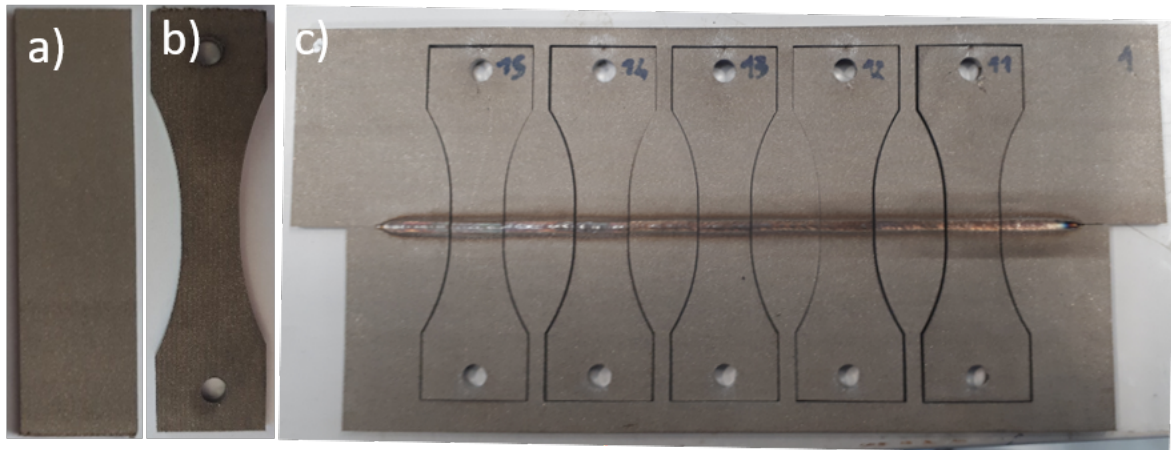


FIGURE 6: Final specimens extracted from the a) and b) whole LPBF parts and c) welded parts. For c), two LPBF plates are welded and specimens are extracted by laser cutting.

Hardness measurements were also conducted in cross section along the length and thickness of both materials, after welding and Heat Treatment (HT), and detailed in [17]. A summary of the

results is recalled in Table.4. The LPBF process Base Metal (BM) has higher hardness values than that of the rolled sheet at its BM. However, at the Heat Affected Zone (HAZ) and the Melting Zone (MZ), the hardness values are similar for both rolled and LPBF process batches, since the materials have undergone the same welding treatment. These measurements raise the question of how would the welded LPBF process parts react under fatigue, and will there be competition between crack initiation at the weld seam where the hardness is lowest, or at the BM due to the high roughness levels and the potential manufacturing defects. This question will be answered further in the text.

TABLE 4: Hardness properties of the SS 316L at the rolled and LPBF states [17].

	LPBF base metal	LPBF welded zone	Rolled base metal	Rolled welded zone
Hardness (HV1)	238±6	197±5	166±6	190±6

2.2. Experimental fatigue procedure

All fatigue tests are carried out on a servo-hydraulic Instron 8801 machine, using the Locati method as detailed in the work of Maxwell and Nicholas [21], with 3 specimens per batch. The following conditions are applied :

- Frequency : $f = 25$ Hz.
- Ambient temperature and pressure, in ambient air.
- Load R-ratio : $R = 0.1$.
- Number of cycles : $N = 10^6$ cycles.
- Loading amplitude step $S\sigma_a = 20$ MPa.

At the end of the fatigue tests, an equivalent fatigue stress is calculated for each specimen, using Basquin's law and Miner's law [22], taking into account the damage accumulated during the different loading steps (Eq. 1-3). A mean fatigue strength per batch is then determined.

$$\sigma_a = CN^{-1/b} \quad (1)$$

$$D = \sum_{i=1}^m D_i = \sum_{i=1}^m \frac{n_i}{N_i} \leq 1 \quad (2)$$

$$D = \sum_{i=1}^m n_i \left(\frac{\sigma_a}{C} \right)^b \leq 1 \quad (3)$$

With n_i : number of cycles for each step, σ_a the stress amplitude, D the accumulated damage which equals 1 when the specimen breaks, b and C are material parameters.

In this study, 7 batches of specimens, with 3 specimens per batch, are prepared and tested under cyclic loading. These batches split in 2 base metal types, cold rolled or LPBF produced. Half of the batches is of solid specimens and the other half is of LW specimens. Half of the batches is polished to remove LPBF process surface roughness or welding surface geometry and the other half is tested in As-Built and/or as welded surface conditions. The details for the test campaign are shown in Table 5.

The first batch corresponds to the Rolled and Polished (RP) batch, used as a reference condition. The second batch corresponds to the Rolled and Welded (RW) state. The aim of this batch is to assess the impact of surface and internal defects (porosity), as well as the microstructure change on the fatigue strength. The third batch, RWP, offers a polished surface finish compared to the RW batch and aims to erase the surface geometry defects and to understand the influence of microstructure change and/or the porosity on the fatigue strength, compared to the first two batches. The fourth batch corresponds to the Additively Manufactured As-Built samples (AMAB). It represents the reference batch for the LPBF process and is compared to the RP batch in order to identify the difference in fatigue strength between rolling and additive manufacturing. The fifth batch consists of Additively Manufactured Polished samples (AMP), and allows to observe the influence of roughness compared to the AMAB batch. The sixth batch consists of Additively Manufactured Welded samples (AMW) and the seventh batch is for Additively Manufactured Welded and afterwards Polished samples (AMWP). These two batches allow, compared to the AMAB and the AMP batches, to identify the impact of the LW on the fatigue strength. The microstructural changes as well as the surface and internal defects change by the LW are assessed via these two batches. Let's recall that all samples are polished at the edges and along the side walls to avoid

TABLE 5: Summary of the different surface state batches for fatigue testing.

Batch notation	Process	LW	Surface state	Heat treatment	Topography
RP	Rolling	No	Manual polishing	No	
RW	Rolling	Yes	Raw	Yes	
RWP	Rolling	Yes	Manual polishing	Yes	
AMAB	LPBF	No	As built	Yes	
AMP	LPBF	No	Manual polishing	Yes	
AMW	LPBF	Yes	Raw	Yes	
AMWP	LPBF	Yes	Manual polishing	Yes	

any crack initiation in these areas. In addition, since the welding operation alters the specimens thickness at the weld seam (see Fig. 3), the lowest value of the thickness for each specimen is considered for the fatigue tests.

3. Results and analysis

3.1. Fatigue test results

This section presents the results of the fatigue tests carried out in terms of the stress amplitude σ_a . As presented in Table 6, all the fracture sites considered in the following are located at the gauge length of the specimens. Almost no crack initiation occurred at the edge of the specimens. The two specimens where crack initiation occurred at the edge or away from the gauge length are

considered invalid (see Table 6). The fatigue stress amplitude of each batch is shown in Table 6 and in Fig.7. Based on these results, several conclusions are drawn.

Firstly, the fatigue strength of the reference material in the form of a non welded rolled sheet (RP) is of 224 MPa. Second, the fatigue stress amplitude of the rolled and welded batches, in the raw state RW and after polishing RWP, are similar and are of the order of 135 MPa. This allows to conclude that LW degrades the fatigue strength of 316L rolled sheets by approximately 40%.

Then, the additively manufactured and polished specimens, whether welded AMWP or non welded AMP, have a fatigue strength of 130 MPa, and therefore also a reduction of 42% compared to the RP reference batch.

Subsequently, the batches of additively manufactured specimens and in the raw state, with and without LW, AMAB and AMW, exhibit the lowest fatigue strength with a stress amplitude of 95 MPa for the first and 88 MPa for the second, which corresponds to approximately 30% of reduction compared to the additively manufactured and polished batch AMP and 60% of total reduction compared to the reference batch RP. This decrease is clearly linked to the high surface roughness generated by the additive manufacturing process. The welded and the non welded batches have the same fatigue strength as is the case for the polished batches AMP and AMWP. An important result emerges from these last two observations ; LW does not impact the fatigue strength of additively manufactured batches, particularly in the as-built condition. In fact, crack initiation for the AMW batch occurs far from the weld joint, while remaining in the gauge length of the specimens (see Table 6). This result is interesting as it allows to conclude that it could be possible to weld two LPBF process parts without degrading the global fatigue resistance of the assembly. However, after polishing, a competition between crack initiation at the weld joint or far from it occurs. This will be further addressed in the next section.

In order to better understand these levels of fatigue strength, SEM observations are carried on the fracture surface of the different specimens. The damage mechanisms of each batch are thus identified.

TABLE 6: Fatigue tests results for the different batches.

Batch	Loading at failure σ_a (MPa)	Step N°	N_f ($\times 10^5$)	Estimated fatigue strength (MPa)	Topography	Mean fatigue strength/ batch (MPa)
RP	235	6	2.32	234		224
	215	1	9.79	214		
				NV		
RW	160	4	2.33	152		135
	140	2	3	131		
	140	2	4.65	122		
RWP	120	2	6.41	118		136
	160	4	6.44	161		
	140	3	2.42	131		
AMAB	100	2	3.54	92		95
	100	2	8.5	101		
	100	2	3.16	91		
AMP	140	4	7.7	140		130
				NV		
AMW	120	2	8.21	120		88
	100	2	3.29	92		
	100	2	2.87	90		
AMWP	100	2	0.6	83		130
	120	3	9.34	121		
				NV		
	140	3	6.31	138		

NV : Non valid test because of cracking at the edge of the specimen

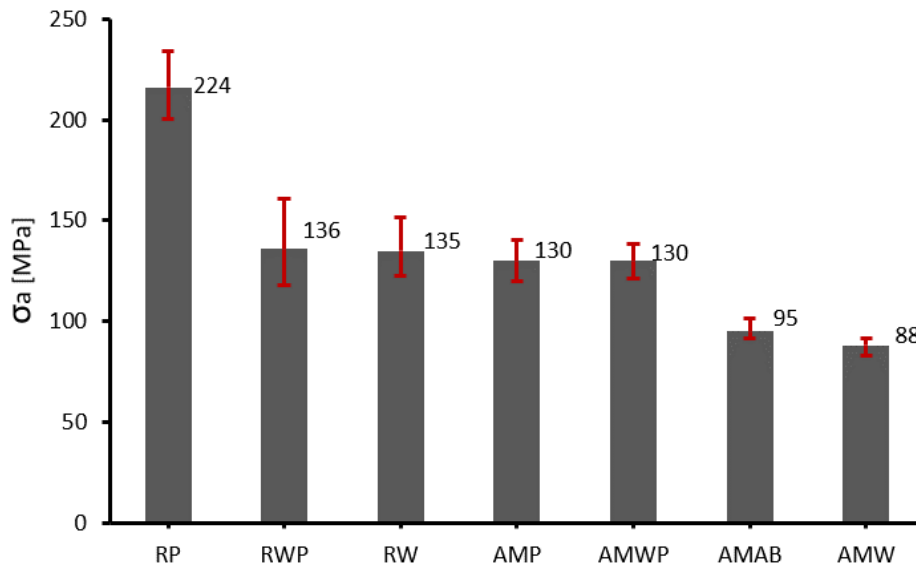


FIGURE 7: Average fatigue strength and the associated extent for each batch.

3.2. Damage mechanisms identification

For the first batch RP, microscopic observations allowed to identify the presence of multiples crack initiation sites (see Fig. 8). These crack initiations are controlled by the plasticity and are always located at the surface of the specimens. No crack initiation on the sub surface or at the bulk is observed. No defects are identified at the crack initiation sites, except small tears and defects that do not exceed $10 \mu\text{m}$ in size (see Fig. 9).

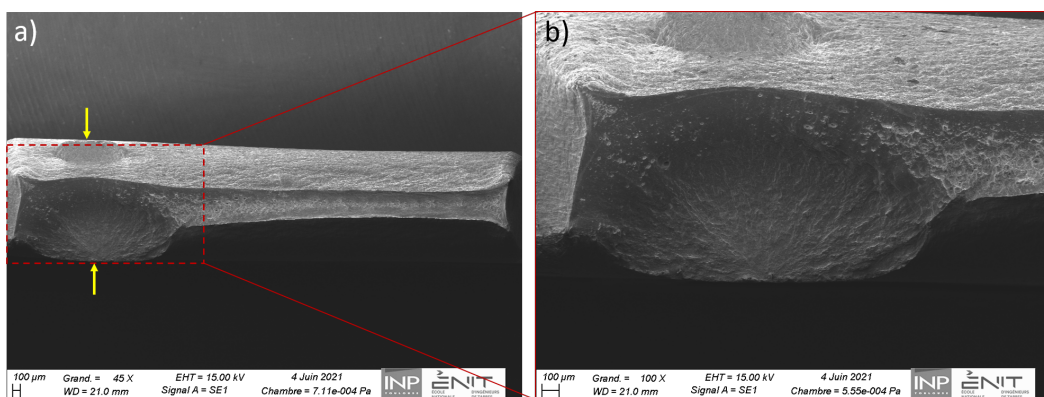


FIGURE 8: Fractography analysis of the specimen 1 of the RP batch : a) multiple cracks identified and b) a zoomed view on the crack propagation area.

For the second batch which is welded RW, SEM observations allowed to identify crack ini-

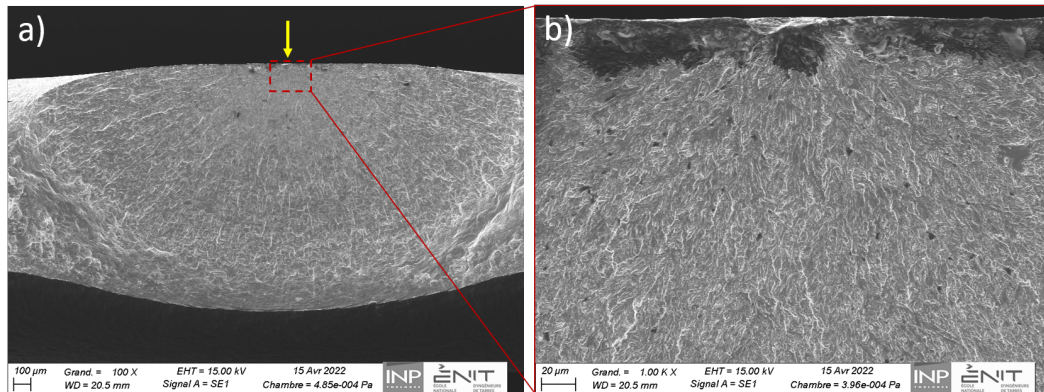


FIGURE 9: Fractography analysis of the specimen 2 of the RP batch : a) defect at the crack initiation site and b) a zoomed view.

tiation at the bottom of the valley of the weld channel (see Fig.10). This is due to the stress concentration generated at the undercuts at the junction between the welded zone and the BM (see Fig. 4). Also, the presence of porosity is identified at the fracture facies, however, no crack initiation occurred at the pores. This can be explained by the fact that the SS 316L is one of the ductile materials for which the HCF initiation of cracks occurs at the surface [23][24]. In addition, the geometry of the weld channel generates higher stress concentrations than those generated by the porosities. This is validated via a FE calculation in 2D domain of 10 mm x 2 mm geometry, in the elastic regime as presented in Fig.11. The calculation is carried out using Abaqus ® software using triangular elements with six nodes and quadratic interpolation function. A convergence study is carried out on a model representing a hole in a plate to identify a suitable mesh size, which varies from 0.01 mm to 0.2 mm. As for the boundary conditions, the simulated domain is under uniform tension loading (Displacement $U_x = 0$ along the line [AB]; Displacement $U_y = 0$ at the point (A); A uniform tensile pressure function is applied along the line [CD]). The geometry of the weld channel is reproduced based on the micrography shown in Fig.11-a. A continuity of the mesh and therefore of the material between the different zones is considered. The material's behavior law used in the model is isotropic linear elastic whether in the BM, HAZ or MZ zone. The gradient of property between the different zones is not modelled. The variation of microstructure as well as its orientation and the anisotropy detailed in [17] is not taken into account. The porosity, simulated by a circular defect, is brought closer to the extreme surface to accentuate its impact.

Nonetheless, the bottom of the weld channel has a much higher stress concentration than that at the porosity. Fig.11 also shows the stress concentration based on normal stress along the loading direction, which is also highest at the bottom of the welding seam. This result allows to explain the crack initiation at this region, as observed on the SEM analysis.

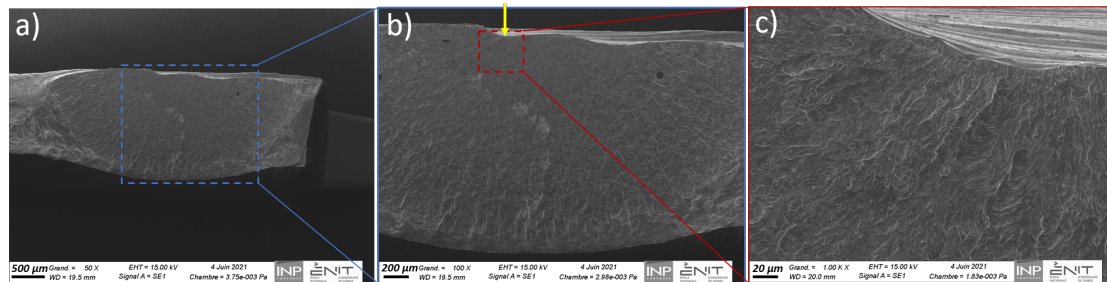


FIGURE 10: Fractography analysis of the specimen 1 of the RW batch : a) crack initiation site and b) and c) zoomed views on the initiation site.

For the third batch, rolled, welded and polished RWP, the polishing operation aimed to remove the geometric shape of the weld bead, in order to identify the impact of the microstructural change induced by LW on the fatigue resistance, compared to the RP reference batch as well as the RW batch. Unfortunately, the defects generated on the sides of the weld beads reached depths of between 100 and 150 μm . The polishing operation did not succeed in removing them completely without the risk of significantly reducing the specimen's thickness and altering fatigue tests results. As a result, the same crack initiation mechanism as well as the same fatigue strength as the previous batch, RW, is found (see Fig.12 and Table 6). With this result, the question remains open on what is the sole effect of the microstructural change, if the surfaces were smooth for RWP state, on the fatigue behavior compared to the RP and the RW states. More fatigue tests with smooth specimens are required, which could not be achieved in this study. However, it would be expected for such state to exhibit a competition between crack initiation in the BM, where the hardness is lower than in the MZ (see Table.4) but more homogeneous microstructure, and in the MZ where the grain size is bigger than in the BM, with interdendritic ferrite structures and where pores are likely to appear due to the welding process. In both cases, if no or small defects are detected at the crack initiation site (around 10 μm), it would be expected a better fatigue strength than the RW batch since large defects are removed. The expected fatigue strength would be similar to or

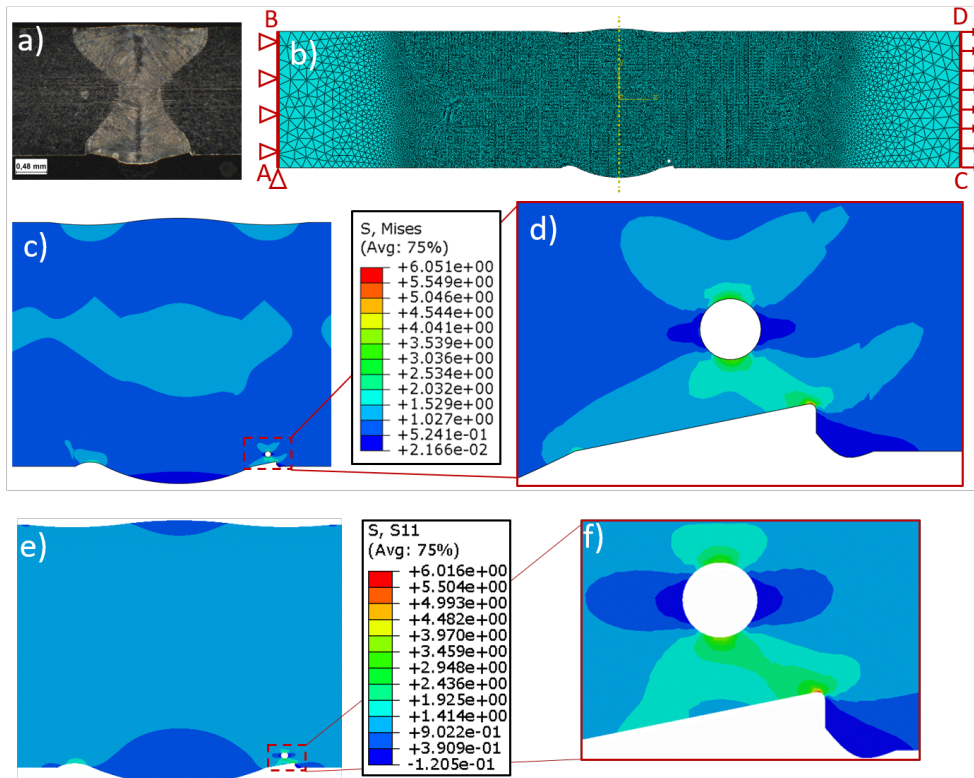


FIGURE 11: a) Geometry of the weld seam, b) 2D geometry, representative of (a) used for FE simulation, c) Mises stress distribution, d) zoom on the maximum stressed area, e) Normal stress distribution along the loading direction and f) zoom on the maximum stressed area. The maximum stress concentration is located at the bottom of the weld seam.

little lower than the RP batch. This assumption is based on the fact that the samples present a microstructural discontinuity and a lower elongation value at the welding zone (see Table.3).

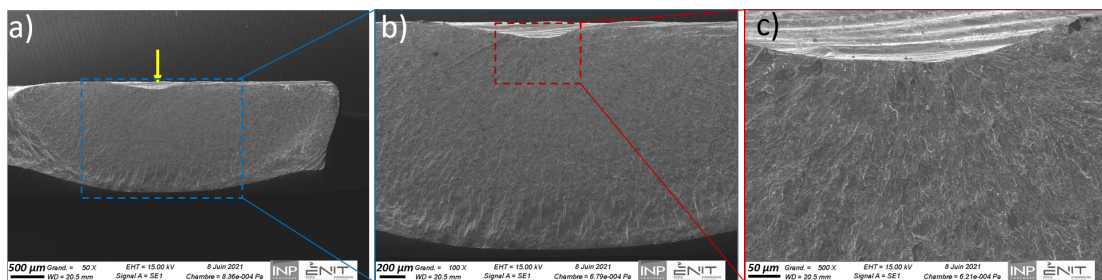


FIGURE 12: Fractography analysis of the specimen 1 of the RWP batch : a) crack initiation site and b) and c) zoomed views.

For the additively manufactured specimens, in the as-built state AMAB, the crack initiation

occurs from a single site for each specimen. Crack initiation is located at the surface of the specimens which exhibit high roughness levels. In addition, at the crack initiation sites, lack of fusion (LoF) defects are identified as shown in Fig.13. In fact, considering a case where the sample shown in Fig.13 has been polished, along the white dotted line in Fig.13-c, the surface roughness would be removed but the LoF defect will persist. This is the case of the following batch, additively manufactured and polished AMP (see Fig.14). For this batch, the analysis of fracture facies shows the presence of a LoF defect at the crack initiation site, as shown in Fig.14.

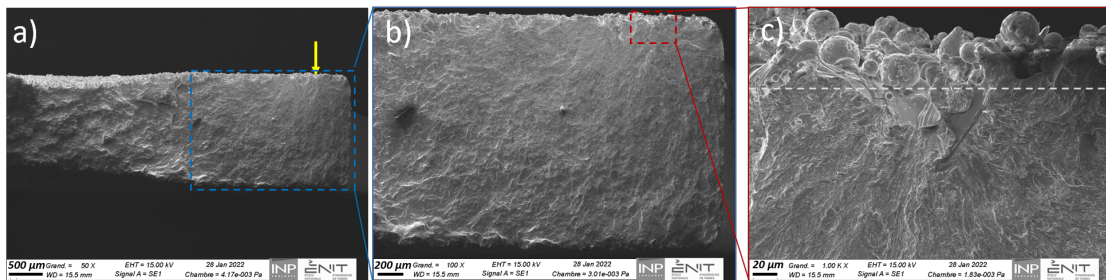


FIGURE 13: Fractography analysis of the specimen 2 of the AMAB batch : a) crack initiation site and b) and c) zoomed views.

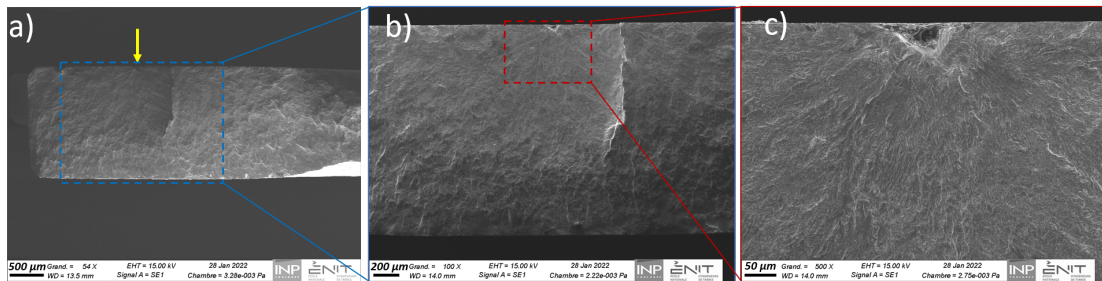


FIGURE 14: Fractography analysis of the specimen 1 of the AMP batch : a) crack initiation site and b) and c) zoomed views.

For the additively manufactured, raw and welded batch AMW, the crack initiation occurs away from the weld bead. Similarly to the AMAB batch, crack initiation is located in areas of high roughness. LoF defects are also identified at the crack initiation sites as shown in Fig.15. This allows to conclude that LW has no significant effect on the fatigue strength of the LPBF process plates in the as-built state. Thus, despite the lower hardness of the MZ compared to the rest of the gauge length of the specimen, the crack systematically initiates in the as-built BM due to the high stress concentration generated by the surface roughness and combined with the LoF defects. The

stress concentration due to the defect therefore has a higher effect than the microstructural effect in this case.

As for the last additively manufactured batch, welded and polished AMWP (see Fig.16), the analysis of fracture surfaces shows a competition between crack initiation from a LoF defect and crack initiation at the bottom of the weld channel (see Fig.16). For the two specimens tested in this batch, crack initiation for the first sample occurred from a LoF defect, as shown in Fig.16-a. However, the second sample shown in Fig.16-b, although polished, has a weld seam undercut that generates the crack responsible for its failure. However, the specimen with a LoF at the crack initiation site had a lower estimated fatigue strength than that cracked at the weld seam (see Table.6).

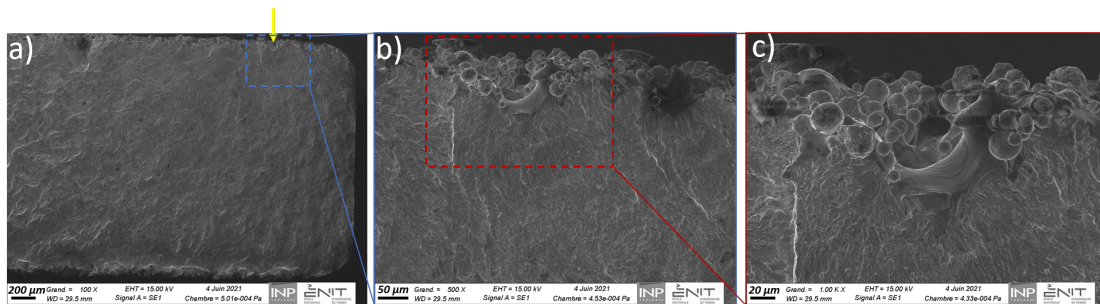


FIGURE 15: Fractography analysis of the specimen 1 of the AMW batch : a) crack initiation site and b) and c) zoomed views.

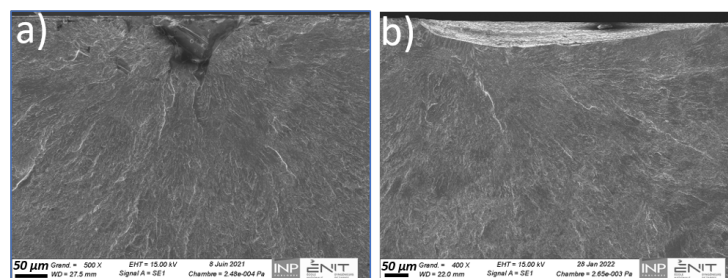


FIGURE 16: Fractography analysis of the specimens of the AMWP batch : a) crack initiation at a LoF defect and b) crack initiation at a weld seam undercut.

Some conclusions can be drawn from these observations. Firstly, for the different studied batches, fatigue crack initiation is a surface phenomenon. No internal crack initiation occurred. This result is in agreement with results of the literature [23] [25]. Secondly, in decreasing order of severity, the stress concentration generated due to surface roughness, combined with the LoF

defects plays the major role, then the sole LoF effect and finally the undercuts at the sides of the welding seams impact the fatigue resistance of the SS 316L. However, in the absence of the surface roughness, a competition between the LoF defects and the welding channel defects appears in the case of the AMWP batch.

3.3. Damage model

Fatigue test results for all batches are plotted in a bi-logarithmic Kitagawa-Takahashi (KT) diagram [26], where the fatigue stress amplitude σ_a is plotted against the square root of defect's projected area in a perpendicular surface to the loading direction \sqrt{area} (see Fig.17). The area of the defects is measured either directly in the case of singular defects, at the initiation sites using the SEM observations (i.e. Fig.15 and Fig.16), or using Murakami's approximation ($\sqrt{area} = \sqrt{10} * a$)[27] in the case of long and shallow defects (i.e. Fig.10).

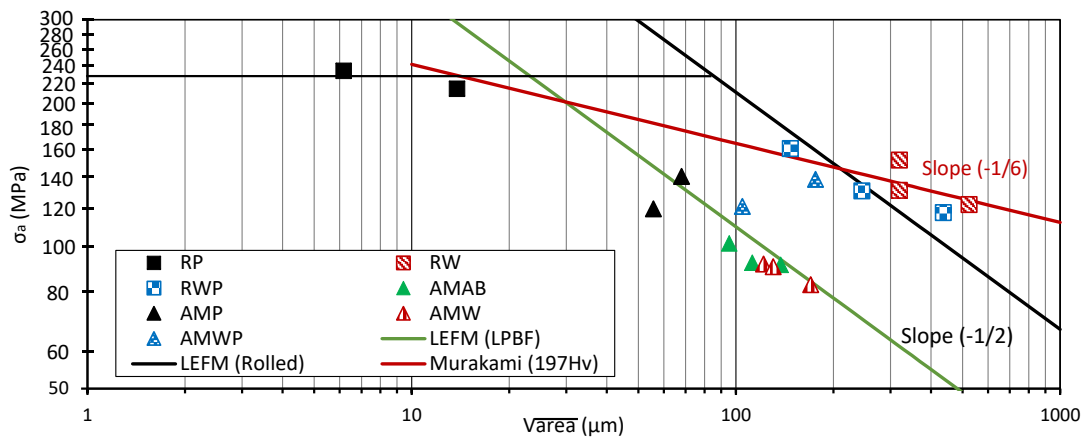


FIGURE 17: KT diagram showing the stress amplitude versus the square root of the defect's area.

Fig.17 shows a classic Kitagawa-Takahashi trend with two distinct regions. First, a plateau for which the fatigue strength is not affected by the presence of defects smaller than a threshold size. Beyond this critical size, a second zone where the fatigue strength is greatly affected by the presence of the defects. Note that the batches obtained from a rolled sheet are presented with squares and those obtained via additive manufacturing are presented with triangles.

At the first glance at Fig.17, a high scatter in the results could be observed, at 120 MPa for example, where the defect sizes range from 55 μm to 500 μm , however, these values belong to

two distinct sets of points, which correspond to two specific damage mechanisms, but more importantly to two manufacturing processes (rolling or additive manufacturing). In other words, the graph shows a separate area for the additively manufactured specimens and another for the rolled specimens. A trend is observed where the slope of the KT diagram is of $-1/2$ for the LPBF process parts, which corresponds to the Linear Elastic Fracture Mechanics (LEFM) model as expressed in Eq. 4. As for the rolled parts, the slope is of $-1/6$ which follows Murakami's model as expressed in Eq. 5. The diagram also allows to identify a threshold size of defects of around $10\text{-}30\ \mu\text{m}$. Furthermore, in Fig.18, results of studies from the literature, for both rolled [28] and LPBF process [25] materials, are added to the diagram and compared with our results. Note that the results of the study of Guerchais et al. [28], conducted using the R-1 ratio, are adapted to the R0.1 ratio using Gerber's relation. The different results show good agreement for both rolled and LPBF process part and allow to confirm, among other things, the difference between the fatigue strength levels and trends.

$$\Delta\sigma_a = \frac{\Delta K_{th}}{Y\sqrt{\pi a}} \quad (4)$$

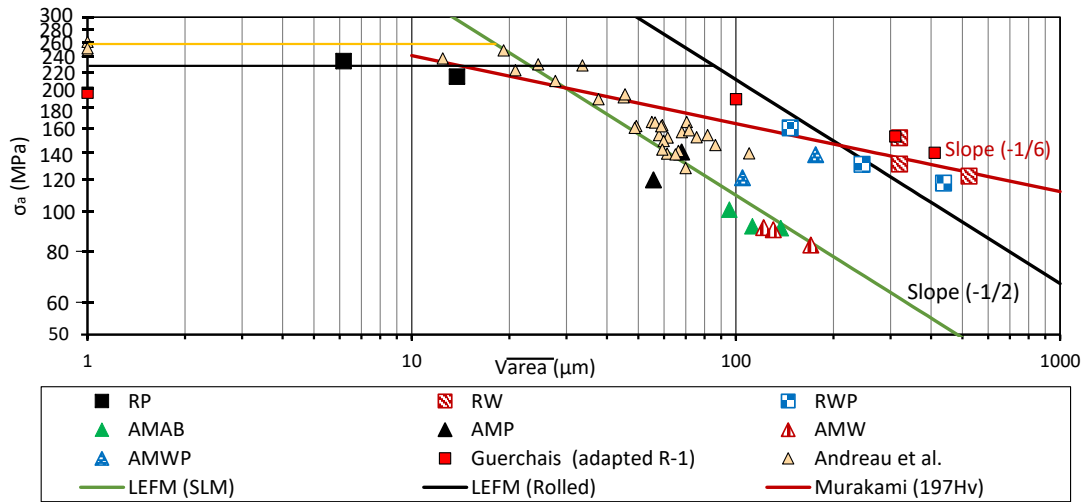


FIGURE 18: KT diagram showing a comparison between our results and the literature [25] [28].

Most of the results of Andreau's study [25] are located, in the KT diagram, between $10\ \mu\text{m}$ and $60\ \mu\text{m}$, which corresponds to the zone of competition between the effects of defects and microstructure on the fatigue strength. Andreau's results show that in the absence of defects, the

LPBF process material exhibits a better fatigue strength than the rolled material (fatigue strength of around 254 MPa as shown in Fig.18). They show the possibility of improving material health by optimizing the printing parameters [25]. The present results show that beyond the competition zone between defects and microstructure (zone beyond 60 μm), the decrease in fatigue strength in the presence of defects rather follows a slope of -1/2 for LPBF process parts, against a slope of -1/6 for rolled sheets. This allows to conclude that the LPBF process parts are more sensitive to the presence of defects than the rolled parts. This could be explained by the microstructural difference between the two materials. As shown in Table.3, the LPBF process material exhibits lower elongation than the rolled material, with or without welding, which could be at the origin of this slope difference. The microstructural and elongation differences allow also to explain the scatter issue addressed above.

In addition, Fig. 18 shows that our specimens have bigger defect sizes than the specimens used by Andreau et al., in the case of the additively manufactured parts, which results in a lower fatigue strength for our specimens. Manufacturing parameters vary for the specimens in [25] and our specimens, which could be at the origin of this difference. However, the specimens used in [25] have around half the section and around half the perimeter of the specimens used in the present study, which could result in a scale effect due to the lower probability of creating large defects and hence a better fatigue strength. However, for the rolled parts, the fatigue strength obtained in our study and that obtained by Guerchais et al. [28] are close despite the fact that the specimens used in [28] are much bigger, in terms of section and perimeter, than the specimens used in this study. This could suggest that the LPBF process parts exhibit a higher sensitivity to the scale effect than that of the rolled parts.

Another interesting result is the case of the AMWP batch where two specimens shows different damage mechanisms and different fatigue strengths. Fig.17 shows that the smaller \sqrt{area} caused more effect in the fatigue strength. This could be explained by the stress concentration generated at the LoF defects which is often higher than that generated at the weld seam due to their shape (see Fig.16-a). The AMWP specimen that breaks from the weld seam is located among the rolled batches in Fig.17. This is due to the fact that the initiation occurs in the MZ, which has the same mechanical characteristics and hardness for both LPBF process and rolled batches.

On the same graph in Fig.17 and Fig.18 are presented the fatigue behavior predictions via Murakami's model in red line (Eq. 5) and LEFM model in green and black lines (Eq.6).

$$\sigma_a = \frac{1.43(H_v + 120)}{(\sqrt{area})^{1/6}} \left(\frac{1 - R}{2} \right)^\alpha \quad (5)$$

with $\alpha = 0.3$ as identified from experimental results [27].

For the LEFM model, Murakami's approximation for the stress intensity factor is applied, assuming that the cracks propagate in mode I. The fatigue stress amplitude is hence expressed, based on the LEFM, as follows :

$$K = 0.65\sigma \sqrt{\pi \sqrt{area}} \Rightarrow \sigma_a = \frac{\Delta K}{1.3 \sqrt{\pi \sqrt{area}}} \quad (6)$$

Murakami's model is applied using the hardness value for the rolled welded material, of around 197 Hv (see Table.4), whereas the LEFM model is applied using two different values of ΔK_{th} of 1.9 MPa. \sqrt{m} and 3.7 MPa. \sqrt{m} , obtained via the least square method based on the experimental results, for the LPBF process and the rolled parts respectively. The crack closure phenomenon is neglected in this study. It can be seen on the KT diagram that Murakami's model and the LEFM model successfully describe the observed fatigue behavior for the rolled and LPBF process materials, respectively.

4. Conclusion and prospects

The main conclusions of this study can be presented as follows :

- Both LPBF process parts and rolled parts show good weldability with low rate of defects or porosity at the welded zone, However, the weld seam shows undercuts along the width of the specimens.
- LW reduces the fatigue strength of the rolled batches, which is mainly due to the stress concentration at the bottom of the welding channels.
- Compared to the rolled polished 316L (RP), the HCF strength of 316L LPBF process parts decreases by 60% in the as-built state (AMAB and AMW) and by 42% after polishing (AMP and AMWP).

- For welded LPBF process batches, there is no effect of the welding on the fatigue resistance, it is rather the roughness and LoF defects at the surface that drive the fatigue behavior. It is hence possible to weld two additively manufactured parts without degrading the global fatigue strength of the assembly.
- The LPBF process parts exhibit a steeper slope on the KT diagram than that of the rolled parts and are hence more sensitive to defects. The microstructural difference between the rolled and the LPBF process materials could be at the origin of this variation.
- The obtained results are in agreement with results from the literature for both LPBF process and rolled parts. For the rolled parts, the results in presence of welding defects are in agreements with results obtained in presence of artificial defects from [28].
- The obtained fatigue results are presented in the format of the Kitagawa-Takahashi diagram, and the size of the critical defect was identified in the order of 10-30 μm .

This study shows the possibility of assembling LPBF process parts without risking lowering the fatigue strength of the assembly. However, in the as-built state or even after polishing, the fatigue strength of the 316L LPBF process parts is lower than that of the rolled parts, mainly due to the manufacturing defects of LPBF process, such as surface roughness and LoF defects. As prospects of this study, reducing the size and population of LPBF process defects, using post-processing or in-situ techniques will be investigated. The sole impact of the microstructure and the residual stresses will also be studied.

Declarations

- **Authors' contributions** All authors contributed to the study conception and design. Material preparation and data collection were performed by F. Abroug, A. Monnier and Y. Balcaen. Analysis, discussions and validation were performed by F. Abroug, O. Dalverny and L. Arnaud, A. Monnier and Y. Balcaen. The first draft of the manuscript was written by F. Abroug and all authors commented on previous versions of the manuscript. All authors read and approved the final manuscript.
- **Conflicts of interest/Competing interests** The authors have no relevant financial or non-financial interests to disclose.

— **Availability of data and material** All data generated or analyzed during this study are included in the present article.

5. References

- [1] Benoist, V., Arnaud, L., & Baili, M. (2020). A new method of design for additive manufacturing including machining constraints. *The International Journal of Advanced Manufacturing Technology*, 111(1), 25-36.
- [2] Joshi, S. C., & Sheikh, A. A. (2015). 3D printing in aerospace and its long-term sustainability. *Virtual and Physical Prototyping*, 10(4), 175-185.
- [3] Koutiri, I., Pessard, E., Peyre, P., Amlou, O., & De Terris, T. (2018). Influence of SLM process parameters on the surface finish, porosity rate and fatigue behavior of as-built Inconel 625 parts. *Journal of Materials Processing Technology*, 255, 536-546.
- [4] Vayssette, B., Saintier, N., Brugger, C., El May, M., & Pessard, E. (2019). Numerical modelling of surface roughness effect on the fatigue behavior of Ti-6Al-4V obtained by additive manufacturing. *International Journal of Fatigue*, 123, 180-195.
- [5] Bonneric, M., Brugger, C., & Saintier, N. (2020). Investigation of the sensitivity of the fatigue resistance to defect position in aluminium alloys obtained by Selective laser melting using artificial defects. *International Journal of Fatigue*, 134, 105505.
- [6] Le, V. D., Pessard, E., Morel, F., & Edy, F. (2019). Interpretation of the fatigue anisotropy of additively manufactured TA6V alloys via a fracture mechanics approach. *Engineering Fracture Mechanics*, 214, 410-426.
- [7] Wu, A. S., Brown, D. W., Kumar, M., Gallegos, G. F., & King, W. E. (2014). An experimental investigation into additive manufacturing-induced residual stresses in 316L stainless steel. *Metallurgical and Materials Transactions A*, 45(13), 6260-6270.
- [8] DebRoy, T., Wei, H. L., Zuback, J. S., Mukherjee, T., Elmer, J. W., Milewski, J. O., Beese, A. M., Wilsonheid, A., De, A., & Zhang, W. (2018). Additive manufacturing of metallic components—process, structure and properties. *Progress in Materials Science*, 92, 112-224.
- [9] Matilainen, V. P., Pekkarinen, J., & Salminen, A. (2016). Weldability of additive manufactured stainless steel. *Physics Procedia*, 83, 808-817.
- [10] Rautio, T., Mäkikangas, J., Kumpula, J., Järvenpää, A. & Hamada, A. (2020). Laser Welding of Laser Powder Bed Fusion Manufactured Inconel 718 : Microstructure and Mechanical Properties. *KEM*, 883, 234-241.
- [11] Wu, S. C., Hu, Y. N., Duan, H., Yu, C., & Jiao, H. S. (2016). On the fatigue performance of laser hybrid welded high Zn 7000 alloys for next generation railway components. *International Journal of Fatigue*, 91, 1-10.

- [12] Jokisch, T., Marko, A., Gook, S., Üstündag, Ö., Gumenyuk, A., & Rethmeier, M. (2019). Laser welding of SLM-manufactured tubes made of IN625 and IN718. *Materials*, 12(18), 2967.
- [13] Yang, J., Wang, Y., Li, F., Huang, W., Jing, G., Wang, Z., & Zeng, X. (2019). Weldability, microstructure and mechanical properties of laser-welded selective laser melted 304 stainless steel joints. *Journal of Materials Science & Technology*, 35, 1817–1824.
- [14] Rautio, T., Hamada, A., Mäkikangas, J., Jaskari, M., & Järvenpää, A. (2020). Laser welding of selective laser melted Ti6Al4V : Microstructure and mechanical properties. *Materials Today : Proceedings*, 28, 907-911.
- [15] Eibl, M., Sonsino, C. M., Kaufmann, H., & Zhang, G. (2003). Fatigue assessment of laser welded thin sheet aluminium. *International Journal of Fatigue*, 25(8), 719-731.
- [16] Zhang, Y., Hu, X., & Jiang, Y. (2020). Study on the microstructure and fatigue behavior of a laser-welded Ni-based alloy manufactured by selective laser melting method. *Journal of Materials Engineering and Performance*, 29(5), 2957-2968.
- [17] Mokhtari, M., Pommier, P., Balcaen, Y., & Alexis, J. (2021). Laser Welding of AISI 316L Stainless Steel Produced by Additive Manufacturing or by Conventional Processes. *Journal of Manufacturing and Materials Processing*, 5(4), 136.
- [18] ISO 1099 :2017, Metallic materials — Fatigue testing — Axial force-controlled method.
- [19] Salman, O.O., Gammer, C., Chaubey, A.K., Eckert, J., & Scudino, S. (2019). Effect of Heat Treatment on Microstructure and Mechanical Properties of 316L Steel Synthesized by Selective Laser Melting. *Mater. Sci. Eng. A* , 748, 205–212.
- [20] Ronneberg, T., Davies, C. M., & Hooper, P. A. (2020). Revealing relationships between porosity, microstructure and mechanical properties of laser powder bed fusion 316L stainless steel through heat treatment. *Materials & Design*, 189, 108481.
- [21] Maxwell, D. C., & Nicholas, T. (1999). A rapid method for generation of a Haigh diagram for high cycle fatigue. In *Fatigue and Fracture Mechanics : 29th Volume*. ASTM International.
- [22] Miner, M. A. (1945). Cumulative damage in fatigue. *Journal of Applied Mechanics*, Transactions of ASME 12, pages 159–164.
- [23] Pang, J. C., Li, S. X., Wang, Z. G., & Zhang, Z. F. (2013). General relation between tensile strength and fatigue strength of metallic materials. *Materials Science and Engineering : A*, 564, 331-341.
- [24] Le, V. D. (2016). Etude de l'influence des hétérogénéités microstructurales sur la tenue en fatigue à grand nombre de cycles des alliages d'aluminium de fonderie (Doctoral dissertation, Paris, ENSAM).
- [25] Andreau, O., Pessard, E., Koutiri, I., Penot, J. D., Dupuy, C., Saintier, N., & Peyre, P. (2019). A competition between the contour and hatching zones on the high cycle fatigue behaviour of a 316L stainless steel : Analyzed using X-ray computed tomography. *Materials Science and Engineering : A*, 757, 146-159.
- [26] Kitagawa, H., & Takahashi, S. (1976). Applicability of fracture mechanics to very small cracks. *ASM Pro-*

- ceedings of 2nd international conference on mechanical behaviour of materials. Metalspark, Ohio, 627-631.
- [27] Murakami, Y. (2002). *Metal Fatigue : Effects of Small Defects and Nonmetallic Inclusions*," Elsevier Science Ltd. UK.
- [28] Guerchais, R., Morel, F., Saintier, N., & Robert, C. (2015). Influence of the microstructure and voids on the high-cycle fatigue strength of 316L stainless steel under multiaxial loading. *Fatigue & Fracture of Engineering Materials & Structures*, 38(9), 1087-1104.
- [29] Nie, B., Zhao, Z., Liu, S., Chen, D., Ouyang, Y., Hu, Z., Fan, T., & Sun, H. (2018). Very high cycle fatigue behavior of a directionally solidified Ni-base superalloy DZ4. *Materials*, 11(1), 98.